Probing phase transition dynamics of 2D lead halide perovskites with time-resolved optical spectroscopy

Shunran Li[1,2], Bowen Li[1,2], Bochao Xie[1,2], Yingying Ma[1,2], Snigtha Mohanraj[3], Peijun Guo[1,2,*]

[1]Department of Chemical and Environmental Engineering, Yale University, New Haven, CT 06520, USA

[2]Energy Sciences Institute, Yale University, West Haven, CT 06516, USA

[3]Engineering and Science University Magnet School, West Haven, CT 06516, USA

*E-mail: peijun.guo@yale.edu

Abstract

Understanding and manipulating structural phase transitions in soft functional materials are crucial for their fabrication and optoelectronic applications. Here, we investigate the phase transition dynamics of two-dimensional (2D) metal-halide perovskites (MHPs) using time-resolved vibrational-pump visible-probe (VPVP) spectroscopy, where mid-infrared laser pulses are employed to impulsively heat these materials to transition from a low-temperature phase to a high-temperature phase. We focus on three archetypal 2D lead iodide perovskites, which contain organic spacer cations of varying lengths, to explore the fundamental kinetics of the impulsively driven, temperature-induced phase transitions. Our findings reveal that the phase transitions in these materials occur on the microsecond timescale and are largely independent of the organic spacer length, the substrate, while they become faster at higher temperatures. Our results provide key insights into the structural phase transition mechanisms of 2D MHPs, shed light on the operational speed for these materials if their functions involve structural transitions between two phases, and facilitate further exploration of their functional properties in optoelectronic, ferroelectric, and ferromagnetic applications.

Keywords

Metal halide perovskites; structural phase transition; pump-probe spectroscopy

INTRODUCTION

Two-dimensional metal-halide perovskites (2D MHPs) have attracted considerable attention in recent years as promising semiconducting materials for photovoltaic,[1] optoelectronic,[2,3] and spintronic applications.[4] Compared to their three-dimensional (3D) counterparts, 2D MHPs consist of alternating organic and inorganic layers, which offer a high degree of tunability in the number of layers, their structural arrangement, and the choice of organic spacers, which directly influence their electronic properties such as the bandgap.[5] Furthermore, their quantum-well-like structures result in strong quantum and dielectric confinement, leading to large exciton binding energies and tightly bound excitons.[6,7] The unique crystal structure of 2D MHPs provides enhanced environmental stability,[8] strong photoluminescence and electroluminescence,[9,10] and anisotropic carrier transport characteristics.[11] In addition, the wide variety of available organics spacers enables flexible molecular design, allowing for fine-tuning of material properties and engineering of unique functionalities such as ferroelectricity and spin selectivity.[12-14] Recent research has focused extensively on understanding the fundamental properties of energy carriers and structural dynamics in these materials, inspiring a range of advanced optoelectronic applications.[15-17]

Compared to inorganic semiconducting materials such as Si and GaAs, MHPs exhibit notably soft lattice characteristics.[18] In addition, 2D MHPs typically have a more compliable lattice than their 3D counterparts, as evidenced by lower elastic modula.[19] As a result, 2D MHPs are more susceptible to lattice distortions, intrinsic phase transitions, and structural changes in response to external perturbations such as temperature variations or charge carrier excitation. Billing et al. synthesized a series of 2D MHPs and systematically investigated their steady-state phase transitions using differential scanning calorimetry and X-ray crystallography.[20,21] Their study revealed that the phase transition temperature can be tuned by adjusting the length of the organic spacer cations. Other research shows that temperature-induced phase transitions in 2D MHPs can be effectively regulated by the chemistry of the organic spacers.[22,23] Several recent studies have employed time-resolved methods to explore the interactions between photo-excited charge carriers and the soft lattices of 2D MHPs. Time-resolved X-ray diffraction experiments revealed a transient relaxation and ordering of the octahedral framework driven by photo-excited charge carriers.[24] Zhang et al. employed ultrafast electron diffraction to discover a light-induced, ultrafast reduction in antiferro-distortion of the octahedra, showing that the interaction between the electron-hole plasma and the lattice can be regulated by adjusting the rigidity of 2D MHPs.[25]

Despite the critical role of lattice dynamics in 2D MHPs, the fundamental timescales of first-order structural phase transitions in these materials remain elusive. Although time-resolved synchrotron radiation is a powerful tool for probing structural phase transitions in the temporal domain, the intense X-ray or electron pulses used in such studies can cause rapid material degradation, which is a particular concern when studying phase transition dynamics in MHPs. In contrast, time-resolved optical spectroscopy involves lower pump fluences and is a more accessible technique for investigating phase transitions.[26] Previously, vibrational-pump visible-probe spectroscopy (VPVP) in the nanosecond (ns) to microsecond (μs) range has been employed

to resolve the fundamental phase transition dynamics in the prototypical 3D MHP $CH_3NH_3PbI_3$.[26] Here, we extend time-resolved VPVP experiments to investigate the fundamental phase transition dynamics in several archetypal 2D MHPs, which feature varying organic spacer cation lengths. We show that the phase transition occurs on the μs timescale and is largely independent on the organic spacer lengths. Our results complement earlier studies conducted in the quasi-static limit and open avenues for further exploration of phase transition dynamics in the spatiotemporal domain.[23,27,28]

RESULTS AND DISCUSSION

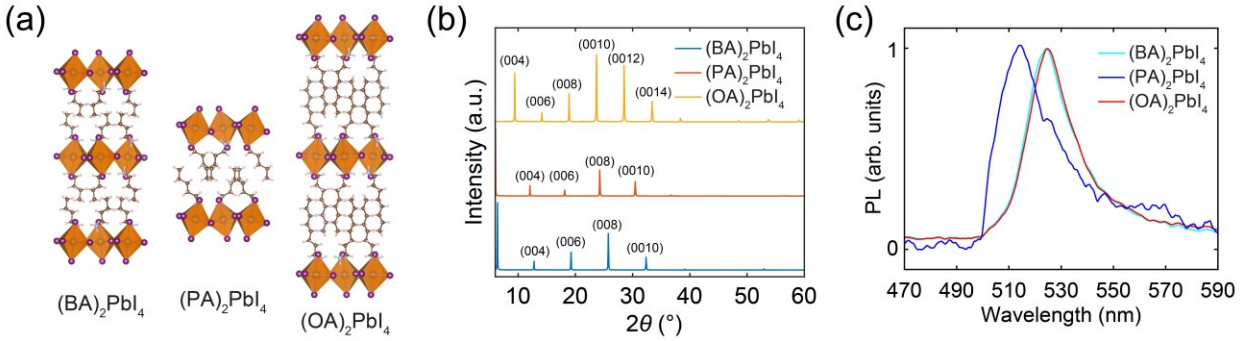

Figure 1. (a) Crystal structures of the three 2D MHPs studied in this work. A single unit cell is shown for each compound. The room-temperature phases are shown for all three compounds. (b) X-ray diffraction patterns of thin films on glass substrate for the three 2D MHPs. (c) Photoluminescence spectra of the three 2D MHP films.

Fig. 1a illustrates the crystal structures of the three 2D MHPs investigated in this work. All three materials are $n = 1$ lead iodide MHPs, each containing organic spacer cations with varying alkyl chain lengths. The compounds can be chemically denoted as $[CH_3(CH_2)_{N-1}NH_3]_2PbI_4$ where $N = 4$ corresponds to butylammonium lead iodide or $(BA)_2PbI_4$, $N = 5$ to pentylammonium lead iodide or $(PA)_2PbI_4$, and $N = 6$ to *n*-octylammonium lead iodide or $(OA)_2PbI_4$. Thin films of these materials were fabricated by hot-casting onto standard glass substrates. Optical microscopy images (Fig. S1) reveal that the films exhibit large grain sizes ranging from microns (μm) to the tens of μm. Based on the interference peaks in the reflectance spectra in the below-bandgap regime (Fig. S2),[29] the thicknesses of the films are estimated to be around 1 μm. X-ray diffraction data (Fig. 1b) confirm a high degree of parallel alignment of the octahedral layers relative to the substrate. Furthermore, photoluminescence (PL) spectra (Fig. 1c) indicate high crystalline quality of the films, as evidenced by the relatively narrow PL peaks centered at excitonic wavelengths near 500 nm for these $n = 1$ lead iodide MHPs.

All three compounds exhibit reversible, first-order structural phase transitions in response to temperature variations.[20,21] Specifically, $(BA)_2PbI_4$ undergoes a transition between two orthorhombic phases (both within the *Pbca* space group) over a temperature range of 223 K to 293 K.[20] This phase transition is characterized by a notable hysteresis, as well as spectral shifts in the

PL peak and exciton absorption onset, which are associated with changes in the electronic bandgap.[30,31] The low-temperature (LT) to high-temperature (HT) phase transition is driven by an order-disorder transition of the BA cations. This change unlocks large-amplitude, anharmonic tilting of the octahedral networks and results in a spectral broadening of the low-wavenumber Raman peaks.[30] In the case of $(PA)_2PbI_4$, three distinct phases have been observed, including two monoclinic phases (space group of $P2_1/a$) at 173 K and 293 K, and an orthorhombic phase (space group of *Pbca*) at 333 K.[20] Our present study for $(PA)_2PbI_4$ focuses on the transition between the monoclinic phase at 293 K and orthorhombic phase at 333 K. For $(OA)_2PbI_4$, our measurements capture all three of its observed phases,[21] including a monoclinic phase (space group of $P2_1/a$) at low temperature, and two orthorhombic phases near and above room temperature (*vide infra*).

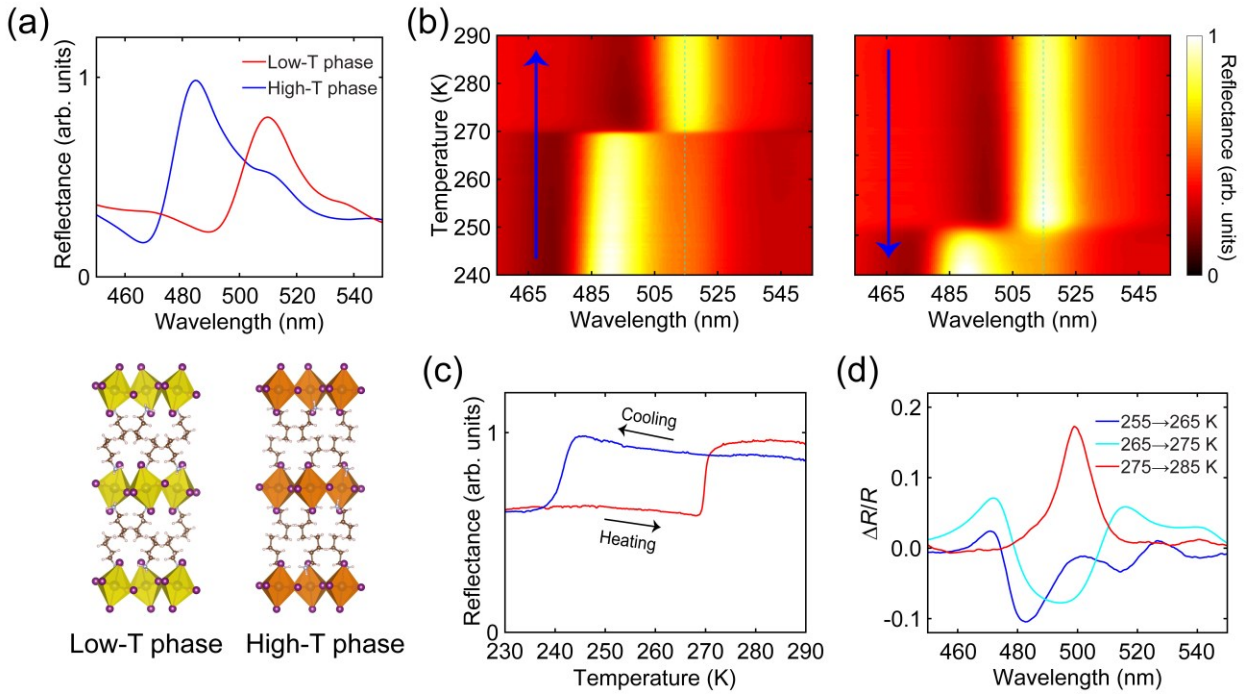

Figure 2. (a) Top: steady-state reflectance spectra for the LT and HT phases of $(BA)_2PbI_4$ (measured at 230 K and 290 K, respectively). Bottom: crystal structures of the LT and HT phases of $(BA)_2PbI_4$. (b) Reflectance intensity map measured during increasing temperature (left) and decreasing temperature (right) shown in arbitrary units. The phase transition temperature is around 269 K along temperature ramp-up and 252 K during temperature ramp-down. (c) Temperature-dependence of the reflectance at 515 nm during temperature cycle showing the abrupt changes associated with the phase transition; data is taken from (b). (d) Differential reflectance spectra, or $\Delta R/R$, calculated using steady-state reflectance spectra at four different temperatures, including 255 K and 265 K in the LT phase, and 275 K and 285 K in the HT phase.

We first focus on our results for $(BA)_2PbI_4$, one of the most widely studied 2D MHPs in the literature.[5,32,33] Since the phase transition temperature of MHP thin films can be influenced by film morphology and substrate-induced strain,[34-36] we characterized the phase transition of our hot-cast

$(BA)_2PbI_4$ film using steady-state optical reflectance spectroscopy at normal incidence. As shown in Fig. 2a, the strong exciton resonance of $(BA)_2PbI_4$, centered at around 500 nm, is manifested as a prominent dip in the reflectance spectrum, accompanied by a peak on the longer wavelength side.[37,38] The reflectance peaks of the LT and HT phases are spectrally separated by approximately 20 nm. Temperature-dependent reflectance spectra reveal a phase transition temperature of approximately 269 K upon heating and 252 K during cooling, indicating a relatively significant hysteresis of 17 K. As illustrated in Fig. 2a (bottom), the LT phase exhibits a lower absorption onset wavelength, giving it a yellower appearance compared to the HT phase.

Importantly, the reflectance maps in Fig. 2b show a significant change in reflectance near the exciton resonance during the phase change. This is further illustrated by the plot in Fig. 2c, which depicts the reflectance at 515 nm, corresponding to the wavelength of the reflectance peak in the HT phase. Based on this observation, we hypothesized that an impulsive thermal excitation, with a sufficient instantaneous temperature rise to induce a phase transition (from the LT to the HT phase), should result in a strong and distinguishable relative change in reflectance, denote as $\Delta R/R$. In steady-state conditions, the $\Delta R/R$ resulting from a temperature variation can be expressed as $[R(T_1) - R(T_0)]/R(T_0)$, where T_1 and T_0 represent two different temperatures. Under this definition, Fig. 2d presents three $\Delta R/R$ curves, calculated using reflectance data at four different temperatures: 255 K and 265 K, where $(BA)_2PbI_4$ resides in the LT phase, and 275 K and 285 K, corresponding to the HT phase. The curves of $\Delta R/R_{255\rightarrow265\ \mathrm{K}}$ and $\Delta R/R_{275\rightarrow285\ \mathrm{K}}$ capture the effects of lattice heating on the reflectance in the LT and HT phases, respectively. $\Delta R/R_{255\rightarrow265\ \mathrm{K}}$ exhibits a derivative-like lineshape skewed toward the negative side, while $\Delta R/R_{275\rightarrow285\ \mathrm{K}}$ displays a prominent positive peak centered around 500 nm. When the exciton resonance of $(BA)_2PbI_4$ is modeled as a damped harmonic oscillator (*i.e.*, using the Lorentzian model), the spectral shapes of $\Delta R/R$ arise from a combination of changes in the damping factor, oscillator strength, and resonance frequency.[39,40] Notably, a distinctively different lineshape is observed for $\Delta R/R_{265\rightarrow275\ \mathrm{K}}$ (going from the LT to HT phase), which features a strong and broad negative dip centered at around 495 nm, with positive lobes on either side, indicative of a prominent bandgap shift.

After establishing the steady-state reflectance properties of $(BA)_2PbI_4$ and observing the distinguishable effects of the phase transition on reflectance, we conducted time-resolved VPVP spectroscopy at varying temperatures. The pump, with a pulse width of ~170 fs, was tuned to a wavelength of 3200 nm, resonant with the C-H and N-H bond stretching vibrations of the BA cations. The broadband probe, with a pulse width of ~1 ns, was delayed by time intervals from a single ns to tens of μs. The pump-induced change in probe reflectance is represented as $\Delta R/R = [R(t) - R(0)]/R(0)$, where $R(t)$ is the probe reflectance at delay time t after the pump, and $R(0)$ is the reflectance without pump excitation. Fig. 3a presents two transient spectral maps of $\Delta R/R$, both obtained at 242 K but under different pump fluences. For the $\Delta R/R$ measured at a lower fluence of 6.6 $mJ \cdot cm^{-2}$, the transient change in reflectance primarily consists of a derivative-like feature spanning the 470 to 490 nm range. When comparing this transient $\Delta R/R$ to the steady-state

analogue obtained within the LT phase (Fig. 2d), we find that the transient $\Delta R/R$ is largely associated with a pump-induced temporary rise in lattice temperature. Notably, $\Delta R/R$ rapidly reaches a maximum following pump excitation, which is due to the fast (nanosecond) thermal equilibration between the excited organic vibrations and the rest of the phonon bath in the material.[41] The subsequent decay in $\Delta R/R$ is a result of temperature decrease as heat dissipates from the $(BA)_2PbI_4$ film into the glass substrate. Additionally, a second, much weaker $\Delta R/R$ feature is observed in the 495~515 nm range, which can be attributed to a minor fraction of the HT phase present in the film dominated by the LT phase.

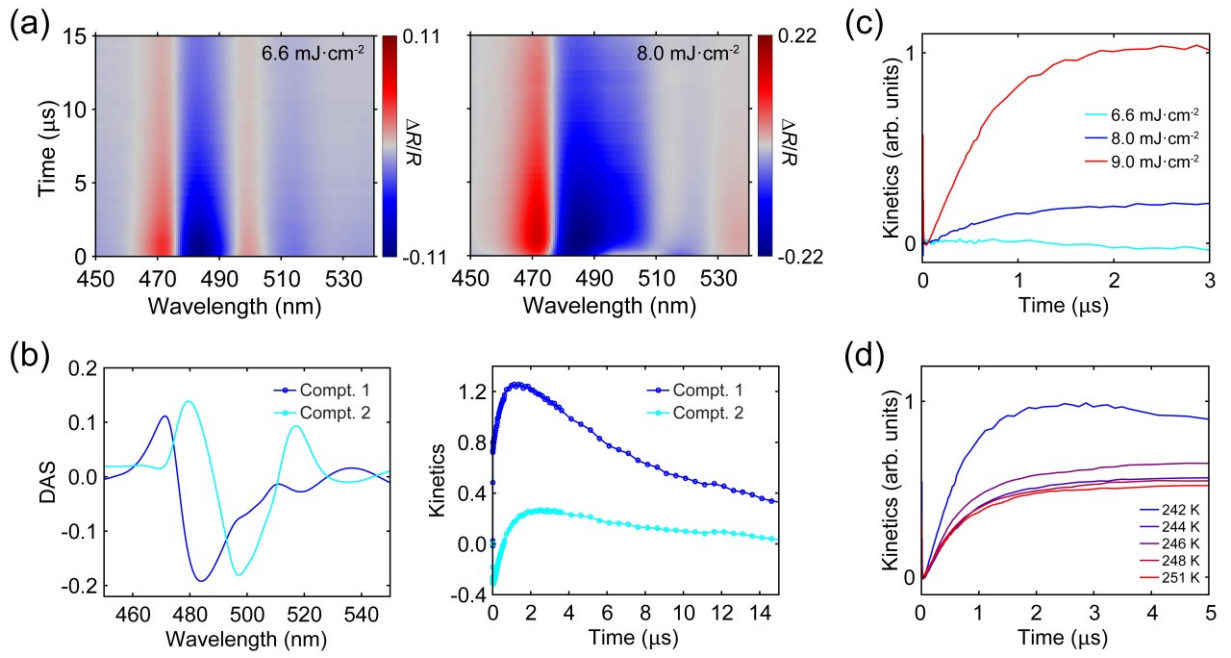

Figure 3. (a) Transient $\Delta R/R$ spectral maps measured at 242 K under pump fluences of 6.6 mJ·cm^{-2} (left) and 8.0 mJ·cm^{-2} (right). (b) Left: decay-associated spectra (DAS) that make up the transient $\Delta R/R$ spectral map measured at 242 K at 8.0 mJ·cm^{-2}. Right: decay kinetics for the two DAS spectral components shown on the left. (c) Kinetics of DAS for the transient $\Delta R/R$ spectral maps measured at 242 K under different pump fluences. (d) Kinetics of DAS for the transient $\Delta R/R$ spectral maps measured varying temperatures (242 to 251 K) under a fixed pump fluence of 9.0 mJ·cm^{-2}.

Interestingly, with a slight increase in pump fluence from 6.6 to 8.0 mJ·cm^{-2}, the $\Delta R/R$ spectral map (Fig. 3a, right) undergoes a significant qualitative change. First, the negative lobe of $\Delta R/R$ broadens, extending to nearly 510 nm on the red side. Additionally, unlike at lower fluence, the $\Delta R/R$ signal does not rise instantaneously after pump excitation; instead, it grows in amplitude over the first few μs, followed by a decay on the tens of μs timescale. To identify and distinguish different processes obtained at the 8.0 mJ·cm^{-2} pump fluence, we performed a global principal component analysis of the transient spectral $\Delta R/R$ data. The analysis, as summarized in Fig. 3b, reveals that two components are needed to adequately reproduce the $\Delta R/R$ data, each with a

distinct timescale and spectral shape. The amplitude of each component as a function of probe wavelength, referred to as the decay-associated spectrum (DAS), is shown in Fig. 3b (left), while their corresponding temporal dynamics are presented in Fig. 3b (right).

By comparing the DAS in Fig. 3b with the steady-state data-derived $\Delta R/R$ spectra shown in Fig. 2d, we find that the first DAS component closely matches $\Delta R/R_{255\rightarrow265\ \mathrm{K}}$, suggesting that it can be attributed to the heating effect of the LT phase. Notably, the second DAS component, which exhibits a symmetric spectral shape with a broad negative lobe at 495 nm and two positive bands on either side, corresponds well with the steady-state spectrum of $\Delta R/R_{265\rightarrow275\ \mathrm{K}}$. Consequently, this second $\Delta R/R$ component can be assigned to a transient phase transition induced by vibrational pump excitation. Examining their temporal dynamics shown in Fig. 3b (right), we observe that the first $\Delta R/R$ component rises within the first 1 μs, while the second $\Delta R/R$ component shows a rise within the first 2 μs. In other words, despite sub-nanosecond lattice temperature rise, the growth of the HT phase occurs relatively slowly compared to other prototypical phase-change materials, such as VO_2 and chalcogenides,[42,43] where large-scale lattice reorganization is involved in their phase transitions. On the other hand, the μs time for the phase transition of $(BA)_2PbI_4$ is still considered fast, requiring time-resolved optical spectroscopy for its observation. This is because the poor thermal conductivity of 2D MHPs likely limits the heat transfer rate to slower than μs, making our observation inaccessible with quasi-static experiments.

We then varied the pump fluences in the VPVP experiments. Fig. 3c shows the kinetics of the $\Delta R/R$ principal component associated with the transient phase transition under three different fluences, focusing on the first 3 μs. In our VPVP experiments, the transient LT-to-HT phase transition is not limited by the rate of heat transfer (in contrast to the HT-to-LT phase transition, which is strongly influenced by heat transfer rate). However, despite a nonlinear increase in the degree of transient phase transition with increasing pump fluence, the time constant for the transient growth of the HT phase remains nearly unchanged (*i.e.*, growth of the HT phase always takes about 2 μs). The relatively weak fluence dependence of the time constant, as shown in Fig. 3c, suggests that the rate of transient phase transition does not strongly depend on transient lattice overheating. One possible explanation for this is that the phase transition proceeds via a heterogeneous nucleation and growth mechanism, potentially occurring at grain and twin boundaries in the 2D MHP films. These boundaries can accommodate the strain induced by the phase transition, thereby lowering the activation energy. The nucleation and growth of the HT phase is inherently slow, as it involves changes in the ordering and hydrogen bonding of the organic cations, as well as the cooperative tilting of the octahedral layers. Additionally, the large hysteresis in the phase transition temperature suggests that the film may exhibit spatial variation in its phase transition temperature, potentially due to strain and defects in the films.[34,44] Consequently, higher pump fluences result in a larger fraction of the film experiencing sufficient overheating to undergo the phase transition.

Additional transient spectral maps of $\Delta R/R$, acquired at different temperatures in the range of 240-257 K are shown in Fig. S3 and S4. Although the steady-state LT-to-HT phase transition,

as shown in Fig. 2b, primarily occurs at 269 K, we found that the pump-induced transient phase transition can only be observed at lower temperatures, ranging from 240 K to about 254 K. This corresponds to the low-temperature side of the hysteresis range for the phase transition. The reason for this is the repetitive nature of the VPVP experiments, which requires the $(BA)_2PbI_4$ film to revert to the LT phase after each pump-induced LT-to-HT phase transition. When the VPVP experimental temperature exceeds 255 K, the HT-to-LT phase transition becomes less likely, as confirmed by the steady-state data shown in Fig. 2b (right), which in turn hinders the VPVP experiments.

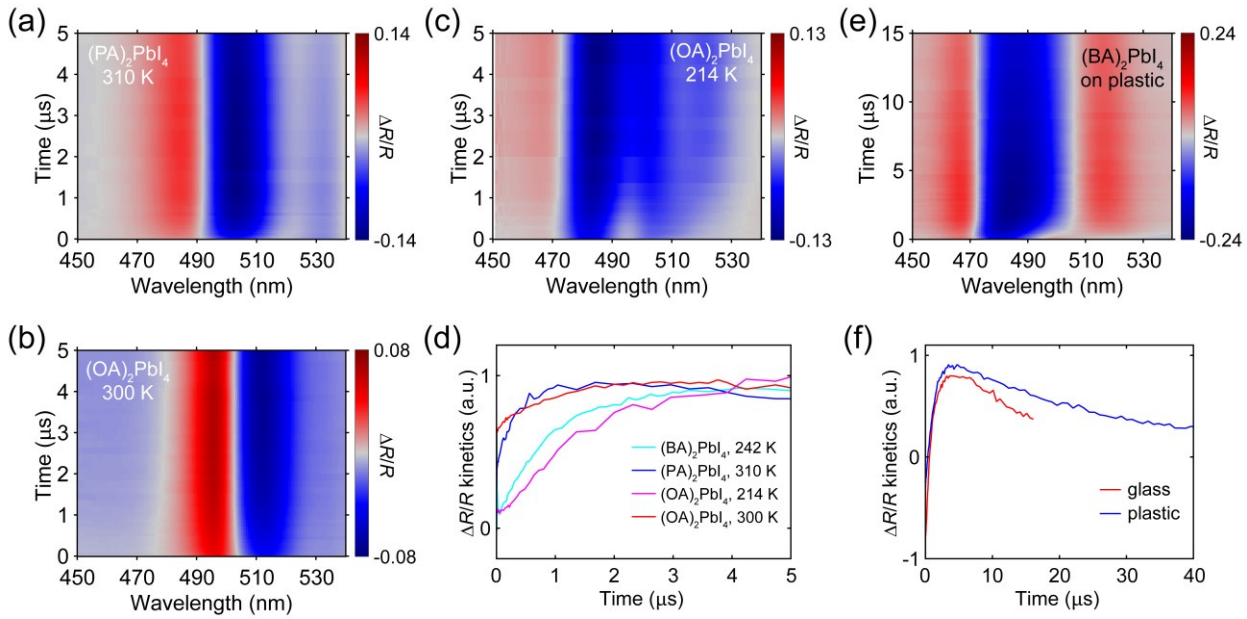

Figure 4. Transient $\Delta R/R$ spectral map for $(PA)_2PbI_4$ measured at 310 K in (a), for $(OA)_2PbI_4$ measured at 300 K in (b), and for $(OA)_2PbI_4$ measured at 214 K in (c). The pump fluence was fixed at 5.2 $mJ \cdot cm^{-2}$ in (a) to (c). (d) $\Delta R/R$ kinetics associated with transient phase transitions of the three compounds measured at different temperatures as indicated in the legend. (e) Transient $\Delta R/R$ spectral map for $(BA)_2PbI_4$ on plastic substrate measured at 100 K with a pump fluence of 3.9 $mJ \cdot cm^{-2}$. (f) $\Delta R/R$ kinetics comparison for transient phase transitions of $(BA)_2PbI_4$ on glass and plastic substrates.

By performing global analysis on the transient $\Delta R/R$ data acquired at different temperatures from 240 to 251 K (Fig. S3 and S4), we obtained the temperature-dependent kinetics of the principal component associated with the pump-induced phase transition, as shown in Fig. 3d. The data reveal a decreasing amplitude of the principal component, which we attribute to the reduced amount of un-transitioned LT phase at higher temperatures, that undergo pump-induced phase transition. Additionally, the phase transition rate slightly decreases with increasing temperature, suggesting that those un-transitioned LT phase requires a higher phase-transition activation energy. At even higher temperatures of 254 and 257 K, we find that the $(BA)_2PbI_4$ film primarily consists of the HT phase, even though these temperatures are significantly lower than the steady-state LT-

to-HT phase transition temperature of 269 K. This is likely due to cumulative pump-induced LT-to-HT phase transitions occurring during the VPVP experiments.

We then performed similar VPVP experiments to investigate the phase transition kinetics of $(PA)_2PbI_4$ and $(OA)_2PbI_4$, with the transient $\Delta R/R$ spectral maps presented in Fig. 4a, 4b and 4c. For $(OA)_2PbI_4$, we explored two phase transitions occurring at different temperatures (Fig. 4b and 4c). The steady-state reflectance maps showing these phase transitions for both compounds are provided in Fig. S5, while more detailed VPVP measurement results at varying temperatures are presented in Fig. S6, S7 and S8. Although the steady-state reflectance data (Fig. S5) indicate that the phase transition-induced shifts in exciton resonance for these two compounds are not as pronounced as that observed for $(BA)_2PbI_4$, abrupt changes in reflectance are still discernible. From these, we were able to identify transient phase transitions in the VPVP experiments. Specifically, in the $\Delta R/R$ spectral maps (Fig. 4a-4c), the signature of phase transition is evident from the growth in $\Delta R/R$ amplitude during the first few microseconds.

In general, the VPVP data across different compounds suggest that phase transitions in these hybrid 2D MHPs are inherently slower than their 3D counterparts, such as $CH_3NH_3PbI_3$, which undergoes an orthorhombic-to-tetragonal phase transition within 100~200 nanoseconds at around 160 K. However, when comparing the phase transition kinetics of the measured 2D MHPs, as shown in Fig. 4d, we observe that the phase transitions take place more rapidly at higher temperatures, including the transitions of $(PA)_2PbI_4$ at 310 K and $(OA)_2PbI_4$ at 300 K. This observation aligns with an Arrhenius-type dependence of phase transition on temperature and is consistent with previous findings of accelerated vibrational coupling between the organic and inorganic sublattices at elevated temperatures in MHPs.[41] Additionally, it mirrors the much faster (~1 ns) tetragonal-to-cubic phase transition of $CH_3NH_3PbI_3$ at above room temperature, compared to its slower orthorhombic-to-tetragonal transition.[45]

Lastly, we examined the effect of substrate on the phase transition kinetics. The rationale is that although glass substrates used in VPVP experiments have relatively low thermal conductivity (1~2 $W \cdot m^{-1} \cdot K^{-1}$), they still act as efficient heat sinks, causing 2D MHP films to dissipate heat on the few μs timescale. This process competes with the photothermally driven LT-to-HT phase transition. Plastic substrates such as poly(methyl methacrylate) (PMMA), with lower thermal conductivity (<0.5 $W \cdot m^{-1} \cdot K^{-1}$), help retain the temperature rise induced by MIR pump excitation. Fig. 4e presents a $\Delta R/R$ transient spectral map for $(BA)_2PbI_4$ deposited on PMMA substrate. In comparison to Fig. 3a, we observe slower heat dissipation. However, despite improved heat retention, the phase transition dynamics, as shown in Fig. 4f for samples on both glass and plastic substrates, remain similar, with transition completing around 5 μs in both cases. This observation suggests that regions not transitioning to the HT phase within the first few μs likely remain in the LT phase, regardless of the thermal "incubation" time, due to a large transition energy barrier.

CONCLUSIONS

In summary, we employed intense MIR pulses to transiently trigger temperature-induced phase transitions in three representative 2D lead-iodide perovskites and resolved the kinetics of these transitions by probing exciton resonance shifts. Our measurements reveal that a threshold pump fluence is required to initiate the phase transition, and the fundamental timescales of thermally induced transitions in 2D MHPs generally fall within the microsecond range. While increasing the pump fluence results in a larger fraction of the film undergoing the phase transition, as indicated by an enhanced $\Delta R/R$ amplitude, it does not significantly affect the transition kinetics. The observed kinetics of LT-to-HT phase transition appear to be intrinsic to the materials and are consistent across samples on glass and plastic substrates. The results indicate that functional properties of 2D MHPs, such as ferroelectricity[46] and ferromagnetism,[47] may involve a relatively long switching times if phase transitions are needed to access and switching on/off these properties. Additionally, our time-resolved spectroscopic findings suggest the potential for spatiotemporal resolution of phase transitions in these materials through pump-probe microscopy with extended delay time windows in the microsecond range.[40]

Materials and Methods

Materials

Lead (II) bromide ($PbBr_2$, 98%) was purchased from TCI Chemicals. Hydrobromic acid (HBr, 48%), dimethyl sulfoxide (DSMO, 99.9%), *N*,*N*-dimethylformamide (DMF, 99.8%), lead (II) iodide (PbI_2, 99.999%), and γ-butyrolactone (GBL, 99%) were obtained from Sigma-Aldrich. Methylammonium iodide (MAI), *n*-butylammonium iodide (BAI), *n*-pentylammonium iodide (PAI) and *n*-hexylammonium iodide (HAI) were purchased from Greatcell Solar Materials. All chemicals were used as received.

Sample fabrication and structural characterization

The 2D-MHP films were fabricated by following the literature-reported hot-casting method.[1,48] The $(BA)_2PbI_4$ precursor was prepared by dissolving 200 mg of BAI and 230 mg of PbI_2 in 0.5 mL DMF. The $(PA)_2PbI_4$ precursor was prepared by dissolving 215 mg of PAI and 230 mg of PbI_2 in 0.5 mL DMF. The $(HA)_2PbI_4$ precursor was prepared by dissolving 229 mg of PAI and 230 mg of PbI_2 in 0.5 mL DMF. The glass substrates were subsequently cleaned in acetone and IPA for 15 min, followed by the treatment with plasma cleaner for 5 min to ensure good solution wettability. The substrates were preheated at 150 ºC and then placed onto the spin-coater. The precursors were dropped onto the substrate and the spin speed was set at 3000 rpm. After spin-coating, the samples were annealed at 100 ºC for 5 min.

Time-resolved, vibrational-pump visible-probe (VPVP) experiments

A fs Yb:KGW laser (Pharos, Light Conversion) was used to pump an MIR optical parametric amplifier (OPA, Orpheus-ONE) generating the vibrational pump pulse at a wavelength of 3300

nm. The Pharos laser, operating at 2 kHz repetition rate, produced pulses at 1030 nm with a pulse duration of 170 fs and pulse energy of 1.5 mJ, of which 0.9 mJ energy is directed into the OPA by a beam splitter. The energy of the output pump pulse could vary from several microjoules (μJ) to tens of μJ. A supercontinuum laser (Leukos) with low timing jittering of 1 ns and 2-kHz repetition rate was employed as the probe source, covering a spectral range from 370 to 1000nm. In VPVP spectroscopy experiments, the probe pulse was focused onto the sample with normal incidence, collected using a 100-mm achromatic lens, and transmitted onto the input slit of a USB spectrometer (AvaSpec-ULS2048CL-EVO, Avantes) with 2 kHz acquisition rate via a multimode optical fiber. The pump pulse, after passing through an optical chopper operating at 1 kHz, was focused onto the sample from the same side as the probe using a 300 mm CaF_2 lens. The pump fluence was varied by a neutral density filter. The pump-probe delay was controlled by a digital delay generator, allowing the variation of delay time from -20 ns to hundreds of μs. The kHz repetition rate of the pump source ensured complete dissipation of the pump-induced heating effect between successive pump pulses.

ASSOCIATED CONTENT

Data Availability Statement

The data that support the plots within this paper and other findings of this study are available from the corresponding authors upon reasonable request.

Supporting Information

The Supporting Information is available free of charge online. Additional discussion of sample fabrication, experimental methods, sample photographs, and optical spectroscopy results.

AUTHOR INFORMATION

Corresponding Author peijun.guo@yale.edu

Author Contributions

P.G. conceived and led the project. S.L. conducted the experiments with assistance from P.G., B.L., B.X. Y.M. and S.M. P.G. and S.L. wrote the manuscript with assistance from B.L.

Notes

The authors declare no competing financial interests.

FUNDING SOURCES

This work is based upon the work supported by the National Science Foundation under Grant DMR-2313648. P.G. acknowledges the partial support from the Air Force Office of Scientific Research under Grant No. FA9550-22-1-0209.

REFERENCES

(1) Tsai, H.; Nie, W.; Blancon, J.-C.; Stoumpos, C. C.; Asadpour, R.; Harutyunyan, B.; Neukirch, A. J.; Verduzco, R.; Crochet, J. J.; Tretiak, S.; et al. High-efficiency two-dimensional Ruddlesden–Popper perovskite solar cells. *Nature* **2016**, *536*, 312-316.

(2) Yuan, M.; Quan, L. N.; Comin, R.; Walters, G.; Sabatini, R.; Voznyy, O.; Hoogland, S.; Zhao, Y.; Beauregard, E. M.; Kanjanaboos, P.; et al. Perovskite energy funnels for efficient light-emitting diodes. *Nat. Nanotechnol.* **2016**, *11*, 872-877.

(3) Qin, C.; Sandanayaka, A. S. D.; Zhao, C.; Matsushima, T.; Zhang, D.; Fujihara, T.; Adachi, C. Stable room-temperature continuous-wave lasing in quasi-2D perovskite films. *Nature* **2020**, *585*, 53-57.

(4) Lu, H.; Wang, J.; Xiao, C.; Pan, X.; Chen, X.; Brunecky, R.; Berry, J. J.; Zhu, K.; Beard, M. C.; Vardeny, Z. V. Spin-dependent charge transport through 2D chiral hybrid lead-iodide perovskites. *Sci. Adv.* **2019**, *5*, eaay0571.

(5) Stoumpos, C. C.; Cao, D. H.; Clark, D. J.; Young, J.; Rondinelli, J. M.; Jang, J. I.; Hupp, J. T.; Kanatzidis, M. G. Ruddlesden–Popper Hybrid Lead Iodide Perovskite 2D Homologous Semiconductors. *Chem. Mater.* **2016**, *28*, 2852-2867.

(6) Saparov, B.; Mitzi, D. B. Organic–Inorganic Perovskites: Structural Versatility for Functional Materials Design. *Chem. Rev.* **2016**, *116*, 4558-4596.

(7) Katan, C.; Mercier, N.; Even, J. Quantum and Dielectric Confinement Effects in Lower-Dimensional Hybrid Perovskite Semiconductors. *Chem. Rev.* **2019**, *119*, 3140-3192.

(8) Smith, I. C.; Hoke, E. T.; Solis-Ibarra, D.; McGehee, M. D.; Karunadasa, H. I. A Layered Hybrid Perovskite Solar-Cell Absorber with Enhanced Moisture Stability. *Angewandte Chemie International Edition* **2014**, *53*, 11232-11235.

(9) Wang, N.; Cheng, L.; Ge, R.; Zhang, S.; Miao, Y.; Zou, W.; Yi, C.; Sun, Y.; Cao, Y.; Yang, R.; et al. Perovskite light-emitting diodes based on solution-processed self-organized multiple quantum wells. *Nat. Photonics* **2016**, *10*, 699-704.

(10) Smith, M. D.; Connor, B. A.; Karunadasa, H. I. Tuning the Luminescence of Layered Halide Perovskites. *Chem. Rev.* **2019**, *119*, 3104-3139.

(11) Guo, P.; Huang, W.; Stoumpos, C. C.; Mao, L.; Gong, J.; Zeng, L.; Diroll, B. T.; Xia, Y.; Ma, X.; Gosztola, D. J.; et al. Hyperbolic Dispersion Arising from Anisotropic Excitons in Two-Dimensional Perovskites. *Phys. Rev. Lett.* **2018**, *121*, 127401.

(12) Li, L.; Shang, X.; Wang, S.; Dong, N.; Ji, C.; Chen, X.; Zhao, S.; Wang, J.; Sun, Z.; Hong, M.; et al. Bilayered Hybrid Perovskite Ferroelectric with Giant Two-Photon Absorption. *J. Am. Chem. Soc.* **2018**, *140*, 6806-6809.

(13) Kim, Y.-H.; Zhai, Y.; Lu, H.; Pan, X.; Xiao, C.; Gaulding, E. A.; Harvey, S. P.; Berry, J. J.; Vardeny, Z. V.; Luther, J. M.; et al. Chiral-induced spin selectivity enables a room-temperature spin light-emitting diode. *Science* **2021**, *371*, 1129-1133.

(14) Long, G.; Jiang, C.; Sabatini, R.; Yang, Z.; Wei, M.; Quan, L. N.; Liang, Q.; Rasmita, A.; Askerka, M.; Walters, G.; et al. Spin control in reduced-dimensional chiral perovskites. *Nat. Photonics* **2018**, *12*, 528-533.

(15) Shi, E.; Yuan, B.; Shiring, S. B.; Gao, Y.; Akriti; Guo, Y.; Su, C.; Lai, M.; Yang, P.; Kong, J.; et al. Two-dimensional halide perovskite lateral epitaxial heterostructures. *Nature* **2020**, *580*, 614-620.

(16) Lai, P.-T.; Chen, C.-Y.; Lin, H.-C.; Chuang, B.-Y.; Kuo, K.-H.; Greve, C. R.; Su, T.-K.; Tan, G.-H.; Li, C.-F.; Huang, S.-W.; et al. Harnessing 2D Ruddlesden–Popper Perovskite with Polar Organic Cation for Ultrasensitive Multibit Nonvolatile Transistor-Type Photomemristors. *ACS Nano* **2023**, *17*, 25552-25564.

(17) Gong, X.; Voznyy, O.; Jain, A.; Liu, W.; Sabatini, R.; Piontkowski, Z.; Walters, G.; Bappi, G.; Nokhrin, S.; Bushuyev, O.; et al. Electron–phonon interaction in efficient perovskite blue emitters. *Nat. Mater.* **2018**, *17*, 550-556.

(18) Ferreira, A. C.; Létoublon, A.; Paofai, S.; Raymond, S.; Ecolivet, C.; Rufflé, B.; Cordier, S.; Katan, C.; Saidaminov, M. I.; Zhumekenov, A. A.; et al. Elastic Softness of Hybrid Lead Halide Perovskites. *Phys. Rev. Lett.* **2018**, *121*, 085502.

(19) Negi, A.; Yan, L.; Yang, C.; Yu, Y.; Kim, D.; Mukherjee, S.; Comstock, A. H.; Raza, S.; Wang, Z.; Sun, D.; et al. Anomalous Correlation between Thermal Conductivity and Elastic Modulus in Two-Dimensional Hybrid Metal Halide Perovskites. *ACS Nano* **2024**, *18*, 14218-14230.

(20) Billing, D. G.; Lemmerer, A. Synthesis, characterization and phase transitions in the inorganic-organic layered perovskite-type hybrids $[(C_nH_{2n+1}NH_3)_2PbI_4]$, $n = 4$, 5 and 6. *Acta Cryst.* **2007**, *B63*, 735-747.

(21) Lemmerer, A.; Billing, D. G. Synthesis, characterization and phase transitions of the inorganic–organic layered perovskite-type hybrids [$(C_nH_{2n+1}NH_3)_2PbI_4$], n = 7, 8, 9 and 10. *Dalton Transactions* **2012**, *41*, 1146-1157.

(22) Cuthriell, S. A.; Malliakas, C. D.; Kanatzidis, M. G.; Schaller, R. D. Cyclic versus Linear Alkylammonium Cations: Preventing Phase Transitions at Operational Temperatures in 2D Perovskites. *J. Am. Chem. Soc.* **2023**, *145*, 11710-11716.

(23) Kingsford, R. L.; Jackson, S. R.; Bloxham, L. C.; Bischak, C. G. Controlling Phase Transitions in Two-Dimensional Perovskites through Organic Cation Alloying. *J. Am. Chem. Soc.* **2023**, *145*, 11773-11780.

(24) Cuthriell, S. A.; Panuganti, S.; Laing, C. C.; Quintero, M. A.; Guzelturk, B.; Yazdani, N.; Traore, B.; Brumberg, A.; Malliakas, C. D.; Lindenberg, A. M.; et al. Nonequilibrium Lattice Dynamics in Photoexcited 2D Perovskites. *Adv. Mater.* **2022**, *34*, 2202709.

(25) Zhang, H.; Li, W.; Essman, J.; Quarti, C.; Metcalf, I.; Chiang, W.-Y.; Sidhik, S.; Hou, J.; Fehr, A.; Attar, A.; et al. Ultrafast relaxation of lattice distortion in two-dimensional perovskites. *Nat. Phys.* **2023**, *19*, 545-550.

(26) Li, S.; Dai, Z.; Kocoj, C. A.; Altman, E. I.; Padture, N. P.; Guo, P. Photothermally induced, reversible phase transition in methylammonium lead triiodide. *Matter* **2023**, *6*, 460-474.

(27) Yin, Z.; Leng, J.; Zhao, C.; Liu, J.; Wu, B.; Jin, S. Defect-Induced Inhomogeneous Phase Transition in 2D Perovskite Single Crystals at Low Temperatures. *ACS Omega* **2021**, *6*, 35427-35432.

(28) Hong, H.; Guo, S.; Jin, L.; Mao, Y.; Chen, Y.; Gu, J.; Chen, S.; Huang, X.; Guan, Y.; Li, X.; et al. Two-dimensional lead halide perovskite lateral homojunctions enabled by phase pinning. *Nat. Commun.* **2024**, *15*, 3164.

(29) Guo, P.; Stoumpos, C. C.; Mao, L.; Sadasivam, S.; Ketterson, J. B.; Darancet, P.; Kanatzidis, M. G.; Schaller, R. D. Cross-plane coherent acoustic phonons in two-dimensional organic-inorganic hybrid perovskites. *Nat. Commun.* **2018**, *9*, 2019.

(30) Menahem, M.; Dai, Z.; Aharon, S.; Sharma, R.; Asher, M.; Diskin-Posner, Y.; Korobko, R.; Rappe, A. M.; Yaffe, O. Strongly Anharmonic Octahedral Tilting in Two-Dimensional Hybrid Halide Perovskites. *ACS Nano* **2021**, *15*, 10153-10162.

(31) Ziegler, J. D.; Lin, K.-Q.; Meisinger, B.; Zhu, X.; Kober-Czerny, M.; Nayak, P. K.; Vona, C.; Taniguchi, T.; Watanabe, K.; Draxl, C.; et al. Excitons at the Phase Transition of 2D Hybrid Perovskites. *ACS Photonics* **2022**, *9*, 3609-3616.

(32) Wu, X.; Trinh, M. T.; Zhu, X. Y. Excitonic Many-Body Interactions in Two-Dimensional Lead Iodide Perovskite Quantum Wells. *J. Phys. Chem. C* **2015**, *119*, 14714-14721.

(33) Guo, Z.; Wu, X.; Zhu, T.; Zhu, X.; Huang, L. Electron–Phonon Scattering in Atomically Thin 2D Perovskites. *ACS Nano* **2016**, *10*, 9992-9998.

(34) Steele, J. A.; Jin, H.; Dovgaliuk, I.; Berger, R. F.; Braeckevelt, T.; Yuan, H.; Martin, C.; Solano, E.; Lejaeghere, K.; Rogge, S. M. J.; et al. Thermal unequilibrium of strained black $CsPbI_3$ thin films. *Science* **2019**, *365*, 679-684.

(35) Li, D.; Wang, G.; Cheng, H.-C.; Chen, C.-Y.; Wu, H.; Liu, Y.; Huang, Y.; Duan, X. Size-dependent phase transition in methylammonium lead iodide perovskite microplate crystals. *Nat. Commun.* **2016**, *7*, 11330.

(36) Stavrakas, C.; Zelewski, S. J.; Frohna, K.; Booker, E. P.; Galkowski, K.; Ji, K.; Ruggeri, E.; Mackowski, S.; Kudrawiec, R.; Plochocka, P.; et al. Influence of Grain Size on Phase Transitions in Halide Perovskite Films. *Adv. Energy Mater.* **2019**, *9*, 1901883.

(37) Yaffe, O.; Chernikov, A.; Norman, Z. M.; Zhong, Y.; Velauthapillai, A.; van der Zande, A.; Owen, J. S.; Heinz, T. F. Excitons in ultrathin organic-inorganic perovskite crystals. *Phys. Rev. B* **2015**, *92*, 045414.

(38) Blancon, J. C.; Stier, A. V.; Tsai, H.; Nie, W.; Stoumpos, C. C.; Traoré, B.; Pedesseau, L.; Kepenekian, M.; Katsutani, F.; Noe, G. T.; et al. Scaling law for excitons in 2D perovskite quantum wells. *Nat. Commun.* **2018**, *9*, 2254.

(39) Li, S.; Li, X.; Kocoj, C. A.; Ji, X.; Yuan, S.; Macropulos, E. C.; Stoumpos, C. C.; Xia, F.; Mao, L.; Kanatzidis, M. G.; et al. Ultrafast Excitonic Response in Two-Dimensional Hybrid Perovskites Driven by Intense Midinfrared Pulses. *Phys. Rev. Lett.* **2022**, *129* , 177401.

(40) Li, B.; Xu, J.; Kocoj, C. A.; Li, S.; Li, Y.; Chen, D.; Zhang, S.; Dou, L.; Guo, P. Dual-Hyperspectral Optical Pump–Probe Microscopy with Single-Nanosecond Time Resolution. *J. Am. Chem. Soc.* **2024**, *146*, 2187-2195.

(41) Guo, P.; Mannodi-Kanakkithodi, A.; Gong, J.; Xia, Y.; Stoumpos, C. C.; Cao, D. H.; Diroll, B. T.; Ketterson, J. B.; Wiederrecht, G. P.; Xu, T.; et al. Infrared-pump electronic-probe of

methylammonium lead iodide reveals electronically decoupled organic and inorganic sublattices. *Nat. Commun.* **2019**, *10*, 482.

(42) Zhang, W.; Mazzarello, R.; Wuttig, M.; Ma, E. Designing crystallization in phase-change materials for universal memory and neuro-inspired computing. *Nat. Rev. Mater.* **2019**, *4*, 150-168.

(43) Shao, Z.; Cao, X.; Luo, H.; Jin, P. Recent progress in the phase-transition mechanism and modulation of vanadium dioxide materials. *NPG Asia Mater.* **2018**, *10*, 581-605.

(44) Dobrovolsky, A.; Merdasa, A.; Unger, E. L.; Yartsev, A.; Scheblykin, I. G. Defect-induced local variation of crystal phase transition temperature in metal-halide perovskites. *Nat. Commun.* **2017**, *8*, 34.

(45) Leonard, A. A.; Diroll, B. T.; Flanders, N. C.; Panuganti, S.; Brumberg, A.; Kirschner, M. S.; Cuthriell, S. A.; Harvey, S. M.; Watkins, N. E.; Yu, J.; et al. Light-Induced Transient Lattice Dynamics and Metastable Phase Transition in $CH_3NH_3PbI_3$ Nanocrystals. *ACS Nano* **2023**, *17*, 5306-5315.

(46) Zhang, H.-Y.; Zhang, Z.-X.; Song, X.-J.; Chen, X.-G.; Xiong, R.-G. Two-Dimensional Hybrid Perovskite Ferroelectric Induced by Perfluorinated Substitution. *J. Am. Chem. Soc.* **2020**, *142*, 20208-20215.

(47) Smith, R. T.; Walsh, K. M.; Jiang, Q.; Chu, J.-H.; Gamelin, D. R. An Air-Stable and Exfoliable Ferromagnetic Two-Dimensional Perovskite, $(Phenethylammonium)_2CrCl_4$. *Chem. Mater.* **2024**, *36*, 1571-1578.

(48) Rahil, M.; Ansari, R. M.; Prakash, C.; Islam, S. S.; Dixit, A.; Ahmad, S. Ruddlesden–Popper 2D perovskites of type $(C_6H_9C_2H_4NH_3)_2(CH_3NH_3)_{n-1}Pb_nI_{3n+1}$ ($n = 1$-4) for optoelectronic applications. *Sci. Rep.* **2022**, *12*, 2176.